

Impact of Broken Inversion Symmetry on Molecular States in multi-Weyl fermions

W.C. Silva,^{1,*} J.E. Sanches,¹ D.S. Rojo,¹ L. Squillante,²

M. de Souza,² M.S. Figueira,³ I.A. Shelykh,⁴ E. Marinho Jr.,^{1,†} and A.C. Seridonio^{1,‡}

¹São Paulo State University (Unesp), School of Engineering,

Department of Physics and Chemistry, 15385-007, Ilha Solteira-SP, Brazil

²São Paulo State University (Unesp), IGCE, Department of Physics, 13506-970, Rio Claro-SP, Brazil

³Instituto de Física, Universidade Federal Fluminense, 24210-340, Niterói, Rio de Janeiro, Brazil

⁴Science Institute, University of Iceland, Dunhagi-3, IS-107, Reykjavik, Iceland

We study inversion-symmetry (IS) breaking in impurity dimers coupled to topological multi-Weyl systems in the low-energy dispersion domain. In the IS-preserved multi-Weyl semimetal phase, Hubbard bands split into *symmetric* and *antisymmetric molecular-like* subbands. Breaking IS induces a transition to a multi-Weyl metal, lifting the degeneracy of the Weyl node and closing the *pseudogap*. This causes opposite energy shifts: valence-band *symmetric* (*antisymmetric*) subbands red- (blue-) shift, reversing in the conduction band until a degeneracy point. Beyond this threshold, *symmetric* bands flatten near band cutoffs, whereas *antisymmetric* bands form quasi-zero energy modes asymptotically approaching- yet never crossing- the Fermi level. Crucially, identical molecular symmetries maintain nondegeneracy even as energy separation vanishes with stronger IS breaking. Our results demonstrate symmetry-selective mechanisms for topological molecular states in multi-Weyl systems.

Introduction- Multi-Weyl semimetals [1–4] represent a topological generalization of conventional Weyl semimetals [5–10], being distinguished by higher topological charges ($J > 1$) and associated phenomena such as chiral anomalies, nonlinear optical responses, topological Fano interference, anomalous thermoelectric transport, and Hall effects [11–25]. These systems reveal highly anisotropic low-energy dispersions with relativistic linear scaling ($E \propto \pm v_F k_z$) along a high-symmetry axis, and quadratic or higher-power law scaling ($E \propto \pm \alpha k_{\perp}^J$) in the orthogonal plane ($k_{\perp} = \sqrt{k_x^2 + k_y^2}$), and J denotes the integer topological charge [2], related to the Chern number $C = \pm J$ through the Berry flux $\Phi_B = \oint_S \mathbf{\Omega} \cdot d\mathbf{S} = s2\pi J$, where $\mathbf{\Omega}$ is the Berry curvature and $s = \pm 1$ are the chirality indexes [7]. Multi-Weyl nodes manifest themselves as momentum-space monopole-antimonopole pairs with quantized Berry fluxes $\pm 2\pi J$. Their opposite chiralities act as momentum-space sources and sinks, connected via topologically protected Fermi arc surface states [7, 8].

The topological charge J originates from the merging of J co-chiral Weyl nodes under C_{2J} rotational symmetry protection ($J \leq 3$) [1]. Furthermore, the bulk-boundary correspondence enforces J Fermi arcs per surface projection [2]. The prototypical realizations include HgCr_2Se_4 and SrSi_2 (double-Weyl, $J = 2$) [1, 3, 20, 21] and $\text{A}(\text{MoX})_3$ ($\text{A} = \text{Rb}, \text{Tl}$; $\text{X} = \text{Te}$, triple-Weyl, $J = 3$) [4]. These materials exemplify the interplay between crystalline symmetries (C_4, C_6) and band topology, stabilizing exotic quasiparticles (multi-Weyl fermions) beyond the Standard Model and providing platforms to explore quantum anomalies and correlated topological phases.

A promising route to probe emergent phenomena in

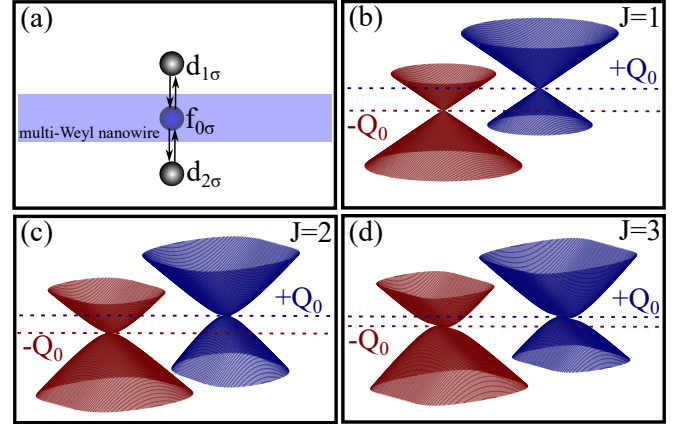


Figure 1. (Color online) (a) A multi-Weyl nanowire featuring a dimer of side-coupled impurities as the prototype system for observing our findings: a specific IS-breaking perturbation $Q_0 \neq 0$ induces degeneracy between the centers of *symmetric* and *antisymmetric* Hubbard *molecular-like* subbands. Beyond the threshold, the *antisymmetric* centers migrate toward the Fermi level without crossing it, forming a pair of quasi-zero energy modes, while the *symmetric* counterparts shift diametrically away, as in Figs.2 and 3. Band structures corresponding to (b) $J = 1$ (single), (c) $J = 2$ (double) and (d) $J = 3$ (triple) Weyl metals exhibiting broken IS.

multi-Weyl systems is by the introduction of magnetic impurities, as this reveals certain fundamental mechanisms governed by these quasiparticles, in particular the synergy between topology and strong electron correlations. Key examples include Kondo single-impurity and lattice systems [28–31], as well as the two-impurity problem characterized by the Ruderman-Kittel-Kasuya-Yosida (RKKY) mediated interaction [32–36]. These systems demonstrate how the enhanced topological charges of multi-Weyl semimetals reshape well-established many-body phenomena.

* corresponding author: willian.carvalho@unesp.br

† corresponding author: enesio.marinho@unesp.br

‡ corresponding author: antonio.seridonio@unesp.br

In this work, we extend previous studies that use impurities as topological probes by exploring emergent regimes beyond the Kondo and RKKY frameworks. We focus on the Coulomb blockade regime [17, 37–39], investigating a dimer of impurities coupled to inversion symmetry (IS)-broken topological multi-Weyl systems in the domain of low energy excitations [Fig.1], where novel quantum molecular states appear.

Starting with the case of intact IS, we observe the formation of *symmetric* and *antisymmetric* Hubbard *molecular-like* subbands. Breaking of the IS shifts Weyl nodes, closes the *pseudogap* characteristic for the semimetallic regime, and drives the system into a Weyl metal phase with renormalized subbands. The *symmetric* (*antisymmetric*) subband undergoes redshift (blueshift) in the valence band and blueshift (redshift) in the conduction band until degeneracy at a specific IS-breaking threshold. Beyond this threshold, *symmetric* subbands shift away from the Fermi level, revealing a pronounced broadening, while *antisymmetric* subbands, playing the role of quasi-zero energy modes, asymptotically approaching the Fermi level without crossing it. Importantly, degeneracy arises exclusively between subbands of opposite symmetry, underscoring the symmetry-selective behavior inherent to multi-Weyl systems.

The Model- To analyze a dimer mediated by low-energy multi-Weyl (mW) fermions, we propose the nanowire setup shown in Fig.1(a). We describe the system by the Hamiltonian (setting $\hbar = 1$),

$$\mathcal{H} = \mathcal{H}_{\text{mW}} + \mathcal{H}_{\text{dimer}}, \quad (1)$$

which is consistent with the Anderson-like framework [17, 40].

The first term

$$\mathcal{H}_{\text{mW}} = \sum_{\mathbf{k}s} \psi_{\mathbf{k}s}^\dagger [D(\tilde{k}_-^J \sigma_+ + \tilde{k}_+^J \sigma_-) + v_F k_{zs} \sigma_z - \sigma_0 Q_0] \psi_{\mathbf{k}s} \quad (2)$$

describes itinerant states via the spinor $\psi_{\mathbf{k}s}^\dagger = (c_{\mathbf{k}s\uparrow}^\dagger, c_{\mathbf{k}s\downarrow}^\dagger)$, where $c_{\mathbf{k}s\sigma}^\dagger$ ($c_{\mathbf{k}s\sigma}$) creates (annihilates) an electron with momentum \mathbf{k} , spin $\sigma = \uparrow, \downarrow$ and chirality $s = \pm 1$ for Weyl nodes at energies sQ_0 and $k_{zs} = k_z - sQ$ breaks time reversal symmetry (TRS). Here, $\tilde{k}_\pm = (k_x \pm ik_y)/k_D$ and J denotes the winding number, with $k_D = D/v_F$ ($\pm D$) representing the *Debye-like* momentum (infrared/ultraviolet) band cutoff. The Pauli matrices are given by $\sigma_\pm = \frac{1}{2}(\sigma_x \pm i\sigma_y)$ and σ_z, σ_0 is the identity matrix, the velocity v_F defines the slope of the Weyl cone along k_z .

The topological charge sJ , related to the Berry curvature flux, ensures the appearance of J Fermi arc pairs at the material boundaries due to the bulk-boundary correspondence [2]. The dispersion relation $\varepsilon_{\mathbf{k}s}^\pm = \pm \varepsilon_{\mathbf{k}s} - sQ_0$ ($\varepsilon_{\mathbf{k}s} = v_F \sqrt{k_{zs}^2 + |\tilde{k}_+|^2 J^2 k_D^2}$) splits into the conduction (+) and valence (-) bands, as shown in Figs.1(b)-(d).

The dimer Hamiltonian reads

$$\mathcal{H}_{\text{dimer}} = \sum_{j\sigma} (\varepsilon_{j\sigma} + \frac{U}{2}) n_{j\sigma} + \frac{U}{2} (\sum_{j\sigma} n_{j\sigma} - 1)^2 - \frac{U}{2} + \frac{1}{\sqrt{\mathcal{N}}} \sum_{j\mathbf{k}\sigma s} (v_{\mathbf{k}j} d_{j\sigma}^\dagger c_{\mathbf{k}s\sigma} + \text{H.c.}), \quad (3)$$

where $\varepsilon_{dj\sigma}$ ($j = 1, 2$) are impurity energies, $n_{j\sigma} = d_{j\sigma}^\dagger d_{j\sigma}$ is the number operator, U is the on-site Coulomb repulsion, and $v_{\mathbf{k}j}$ quantifies atom-host coupling.

The system's spectral properties derive from impurity (DOS $_{jj}$) and molecular (*symmetric/antisymmetric*) orbital densities of states. Using the equation-of-motion method [38] for Green's functions (GFs), we analyze the particle-hole symmetric (PHS) regime by: i) setting $\varepsilon_{j\sigma} = \varepsilon_d = -\frac{U}{2}$ to nullify the first term of Eq.(3); ii) assuming $v_{\mathbf{k}j} \approx v$ (local coupling), with $f_{\sigma\sigma} = \frac{1}{\sqrt{\mathcal{N}}} \sum_{\mathbf{k}s} c_{\mathbf{k}s\sigma}$, as depicted in Fig.1(a).

These assumptions render \mathcal{H} invariant under particle-hole transformations $c_{\mathbf{k}s\sigma} \rightarrow c_{-\mathbf{k}s\sigma}^\dagger$ and $d_{j\sigma} \rightarrow -d_{j\sigma}^\dagger$, yielding $\langle n_{j\sigma} \rangle = \frac{1}{2}$ and giving mirror-symmetric spectral profiles. The impurity DOS, $\text{DOS}_{jl} = (-1/\pi) \text{Im} \tilde{\mathcal{G}}_{jl}$ ($j, l = 1, 2$), is given by the time Fourier transform (TFT) of the GF $\mathcal{G}_{jl} = -i\theta(\tau) \langle \{d_{j\sigma}(\tau), d_{l\sigma}^\dagger(0)\} \rangle_{\mathcal{H}}$.

In the Coulomb blockade regime, when the Kondo and RKKY correlations are irrelevant [27–35], one can safely use the Hubbard-I approximation [17, 37–39]. In this way, the diagonal GF ($j = l$) becomes

$$\tilde{\mathcal{G}}_{jj} = \frac{\frac{1}{2}}{[\tilde{g}_{jj}(\varepsilon + \frac{U}{2})]^{-1} - \tilde{g}_{jj}(\varepsilon + \frac{U}{2})[\tilde{t}(\varepsilon - \frac{U}{2})]^2} + \frac{\frac{1}{2}}{[\tilde{g}_{jj}(\varepsilon - \frac{U}{2})]^{-1} - \tilde{g}_{jj}(\varepsilon - \frac{U}{2})[\tilde{t}(\varepsilon + \frac{U}{2})]^2}, \quad (4)$$

where $\tilde{g}_{jj}(\varepsilon \pm \frac{U}{2}) = [\varepsilon \pm \frac{U}{2} - v^2 \tilde{\mathcal{G}}_\sigma^0]^{-1}$ corresponds to single GFs at Hubbard peaks $\varepsilon = \pm \frac{U}{2}$, with

$$\tilde{\mathcal{G}}_\sigma^0 = \sum_s \tilde{\mathcal{G}}_{\sigma s}^0 = \frac{1}{\mathcal{N}} \sum_{\mathbf{k}s} \frac{\varepsilon_s + i0^+}{[\varepsilon_s + i0^+]^2 + \varepsilon_{\mathbf{k}}^2} \quad (5)$$

being the multi-Weyl fermion GF ($\varepsilon_s = \varepsilon + sQ_0$).

Notably, the Hubbard peaks at $\varepsilon = -\frac{U}{2}$ (first term) and $\varepsilon = \frac{U}{2}$ (second term) in Eq.(4) split into *symmetric* and *antisymmetric molecular-like* states (the subbands centers) due to the effective hopping

$$\tilde{t}(\varepsilon \pm \frac{U}{2}) = [1 \mp \frac{U}{2} \tilde{g}_{jj}(\varepsilon \pm \frac{U}{2})] v^2 \tilde{\mathcal{G}}_\sigma^0, \quad (6)$$

which depends on $\tilde{\mathcal{G}}_\sigma^0$ and U . The off-diagonal GF ($j \neq l$)

$$\tilde{\mathcal{G}}_{jl} = \tilde{t}(\varepsilon \pm \frac{U}{2}) \tilde{g}_{jj}(\varepsilon + \frac{U}{2}) \tilde{\mathcal{G}}_{ll} \quad (7)$$

encodes quantum interference between dimer impurities.

For comparison, consider a conventional dimer with atomic energy ε_0 and hopping t : $\mathcal{H}_{\text{dimer}} = \varepsilon_0 \sum_{j\sigma} n_{j\sigma} +$

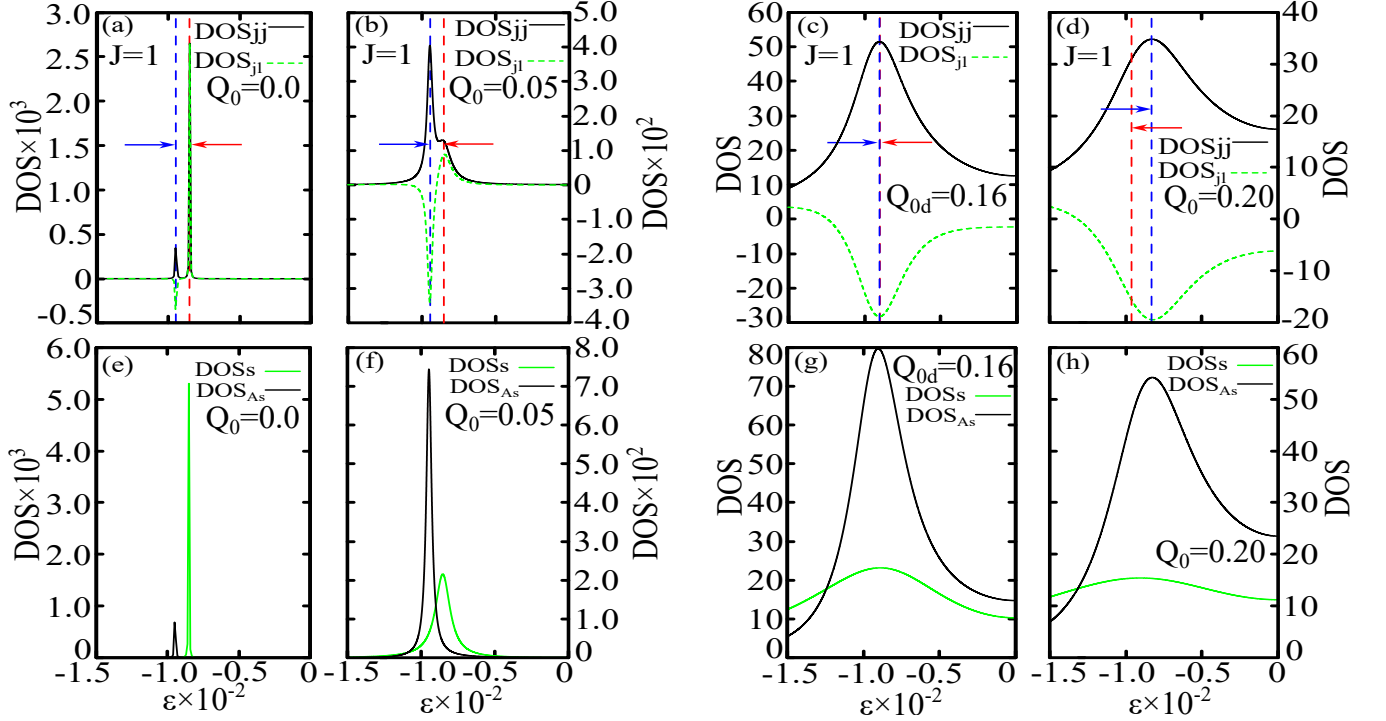


Figure 2. (Color online) Single Weyl PHS analysis: (a)-(d) Diagonal DOS_{jj} and off-diagonal DOS_{ji} spectra in the valence band (negative energies), comparing preserved IS in (a) with progressively broken IS in (b)-(d). In (a), the *antisymmetric* (blue dashed line) and *symmetric* (red dashed line) subbands are clearly resolved. Weak IS breaking in (b) induces partial merging of the subbands via redshift (*symmetric*) and blueshift (*antisymmetric*), as indicated by the arrows. Full coalescence into a degenerate *molecular-like* state occurs at the specific threshold in (c). Beyond this threshold (d), spectral broadening flattens the subband features. (e)-(h) Corresponding *antisymmetric* DOS_{As} and *symmetric* DOS_S profiles under increasing IS breaking. Notably, panel (h) demonstrates a loss of resonance between the subbands as they shift out of alignment.

$\sum_{\sigma} (td_{1\sigma}^{\dagger}d_{2\sigma} + \text{H.c.})$. Here, Eq.(4) reduces to $\tilde{\mathcal{G}}_{jj} = [\varepsilon - \varepsilon_0 + i0^+ - (\varepsilon - \varepsilon_0 + i0^+)^{-1}|t|^2]^{-1}$, yielding molecular energies $\varepsilon - \varepsilon_0 = \pm|t|$ (where $-/+$ corresponds to *symmetric/antisymmetric* states). Analogously, Eq.(4) for our system gives

$$\varepsilon + \frac{U}{2} - \text{Re}[v^2\tilde{\mathcal{G}}_{\sigma}^0] = \pm \text{Re}[\tilde{t}(\varepsilon - \frac{U}{2})] \quad (8)$$

and

$$\varepsilon - \frac{U}{2} - \text{Re}[v^2\tilde{\mathcal{G}}_{\sigma}^0] = \pm \text{Re}[\tilde{t}(\varepsilon + \frac{U}{2})] \quad (9)$$

for split Hubbard subbands centers near $\varepsilon = -\frac{U}{2}$ and $\varepsilon = \frac{U}{2}$, respectively.

The molecular densities of states $\text{DOS}_{S(As)}$ = $(-1/\pi)\text{Im}\tilde{\mathcal{G}}_{S(As)}$ can be derived from the TFT of $\mathcal{G}_{S(As)} = -i\theta(\tau)\langle\{\frac{1}{\sqrt{2}}(d_{1\sigma}(\tau) \pm d_{2\sigma}(\tau)), \frac{1}{\sqrt{2}}(d_{1\sigma}^{\dagger}(0) \pm d_{2\sigma}^{\dagger}(0))\}\rangle_{\mathcal{H}}$, leading to

$$\text{DOS}_{S(As)} = \frac{1}{2} [\text{DOS}_{11} + \text{DOS}_{22} \pm (\text{DOS}_{12} + \text{DOS}_{21})], \quad (10)$$

where $+$ ($-$) denotes *symmetric* (*antisymmetric*) linear combination of the atomic orbitals of the impurities.

To compute $\tilde{\mathcal{G}}_{\sigma}^0$ (Eq.5), we use the *Debye-like* sphere approximation $\mathcal{N} = \sum_{\mathbf{k}s} = \frac{\Omega}{(2\pi)^3} \int d^3\mathbf{k} = \frac{\Omega}{6\pi^2} k_D^3$ and hyperspherical coordinates: $k_x = k_D(\frac{\varepsilon_{\mathbf{k}}\sin\theta}{D})^{1/J} \cos\phi$, $k_y = k_D(\frac{\varepsilon_{\mathbf{k}}\sin\theta}{D})^{1/J} \sin\phi$, $k_{zs} = k_D\frac{\varepsilon_{\mathbf{k}}}{D} \cos\theta$ with Jacobian $J(\varepsilon_{\mathbf{k}}, \theta, \phi) = \frac{k_D^3}{D} (\frac{\varepsilon_{\mathbf{k}}}{D})^{2/J} \frac{(\sin\theta)^{\frac{2}{J}-1}}{J}$ and $\int \tilde{\mathcal{G}}_{\sigma}^0 d^3\mathbf{k} = \int \tilde{\mathcal{G}}_{\sigma}^0 J(\varepsilon_{\mathbf{k}}, \theta, \phi) d\varepsilon_{\mathbf{k}} d\theta d\phi$ [17]. This yields

$$\text{Im}\tilde{\mathcal{G}}_{\sigma}^0 = \sum_s \text{Im}\tilde{\mathcal{G}}_{\sigma s}^0 = - \sum_s \frac{3\pi^{3/2}\Gamma(\frac{1}{J})}{4JD^{\frac{J+2}{J}}\Gamma(\frac{2+J}{2J})} \varepsilon_s^{2/J} = -\pi\rho_0, \quad (11)$$

where $\Gamma(x)$ is the Gamma function. The power law scaling of $\varepsilon_s^{2/J}$ reflects the pristine DOS ρ_0 , which is metallic (finite at the Fermi level) when IS is broken but exhibits a characteristic semimetallic *pseudogap* otherwise.

Using the Kramers-Kronig relation

$$\text{Re}\tilde{\mathcal{G}}_{\sigma}^0 = -\frac{1}{\pi} \int_{-D}^{+D} \frac{\text{Im}\tilde{\mathcal{G}}_{\sigma}^0}{\varepsilon - y} dy, \quad (12)$$

we derive in the wide-band limit [17]

$$\text{Re}\tilde{\mathcal{G}}_{\sigma}^0(J=1) = \sum_s \frac{3\varepsilon_s}{D^3} \left(\frac{1}{2}\varepsilon_s \ln \left| \frac{D+\varepsilon_s}{D-\varepsilon_s} \right| - D \right), \quad (13)$$

$$\text{Re}\tilde{\mathcal{G}}_{\sigma}^0(J=2) = \sum_s \frac{3\pi}{8D^2} \varepsilon_s \ln \frac{\varepsilon_s^2}{|\varepsilon_s^2 - D^2|}, \quad (14)$$

$$\text{Re}\tilde{\mathcal{G}}_{\sigma}^0(J=3) = \sum_s \text{sgn}(\varepsilon_s) \tan(C_{2J}) \text{Im}\tilde{\mathcal{G}}_{\sigma}^0(J=3), \quad (15)$$

where $C_{2J} \equiv 360^\circ/2J$ reflects the rotational symmetry stabilizing multi-Weyl points [1].

Results and Discussion- Within the PHS regime, where $\varepsilon_d = -\frac{U}{2}$ and $v_{\mathbf{k}j} \approx v$, it is sufficient to analyze the spectral properties in the negative energy domain (valence band), as the positive energy region (conduction band) exhibits mirror-symmetric characteristics. Consequently, we further discuss only the first partial fraction in Eq.(4) of $\tilde{\mathcal{G}}_{jj}$ corresponding to the valence band. We fix the parameters to $\varepsilon_d = -0.01D$, $U = 0.02D$, $v = 0.14D$, and $D = 1$ throughout the work.

We first examine the single Weyl case ($J=1$), which displays the diagonal $\text{DOS}_{jj} = (-1/\pi)\text{Im}\tilde{\mathcal{G}}_{jj}$ and off-diagonal $\text{DOS}_{jl} = (-1/\pi)\text{Im}\tilde{\mathcal{G}}_{jl}$ as IS is progressively broken, see Figs.2(a)-(d). The double ($J=2$) and triple ($J=3$) Weyl cases exhibit qualitatively similar behavior, making their explicit presentation unnecessary. The vertical dashed lines in such panels mark the centers of the *molecular-like* subbands, whose positions are determined by numerically solving Eq.(8) for the poles of the GF $\tilde{\mathcal{G}}_{jj}$ [Eq.(4)].

In panel (a) with intact IS ($Q_0 = 0$), DOS_{jl} reveals split Hubbard *molecular-like* subbands in the multi-Weyl semimetal regime: an *antisymmetric* dip (blue dashed line) and a *symmetric* peak (red dashed line) in the vicinity of the original band center $\varepsilon_d = -0.01D$. For DOS_{jj} , the *antisymmetric* subband center corresponds to a peak. This splitting arises from the term $\tilde{t}(\varepsilon - \frac{U}{2})$ in Eq.(6), which introduces energy-dependent hopping mediated by multi-Weyl quasiparticles via $\tilde{\mathcal{G}}_{\sigma}^0$ [Eq.(5)]. In contrast, conventional molecules are characterized by static hopping (determined by wavefunction overlap), which precludes state degeneracy.

When IS is weakly broken ($Q_0 = 0.05D$, panel (b)), the *pseudogap* in Eq.(11) for ρ_0 closes due to the energy shift of the Weyl nodes, signaling the transition to the multi-Weyl metallic phase. Consequently, DOS_{jj} and DOS_{jl} display blue- and redshifted *antisymmetric* and *symmetric* subbands, respectively (see the arrows in Fig.2). These subbands broaden and merge, fully coalescing at $Q_{0d} = 0.16D$ (panel (c)), where their centers align resonantly at the degeneracy point. Here, DOS_{jj} exhibits a single peak, while DOS_{jl} retains a dip. In experimental settings, an application of a stress serves as a means of achieving these novel states as it breaks IS [5]. Furthermore, differential conductance measurements using an STM tip can provide direct access to the DOS_{jj} . For

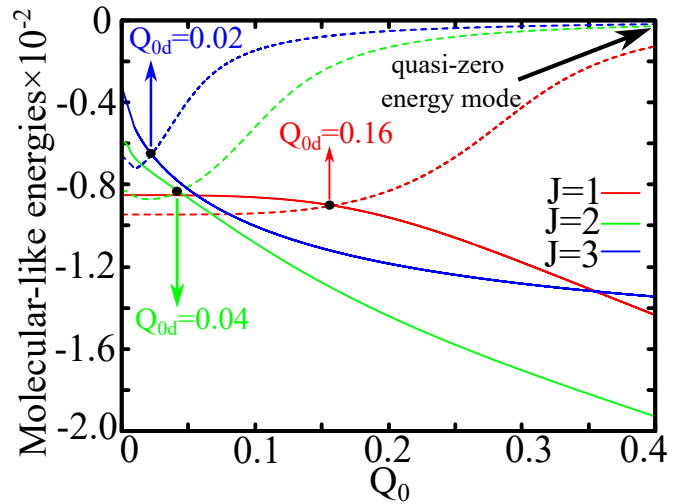


Figure 3. (Color online) Numerical *molecular-like* energies from Eq.(8) as a function of IS breaking parameter Q_0 for single ($J=1$), double ($J=2$) and triple ($J=3$) Weyl fermions in the negative energy domain (valence band). Mirror-symmetric behavior governs the conduction band. The specific thresholds Q_{0d} mark the IS breaking strengths where the *symmetric* and *antisymmetric* subband centers achieve degeneracy. For $Q_0 > Q_{0d}$, the *symmetric* subband center shifts away from the Fermi level, while the *antisymmetric* center asymptotically approaches it. Orbitals with identical symmetry types (e.g., *symmetric/symmetric* or *antisymmetric/antisymmetric*) are prohibited from degenerating, resulting in two quasi-zero energy modes flanking the Fermi level.

$Q_0 > Q_{0d}$ (e.g., $Q_0 = 0.20D$, panel (d)), increased broadening obscures the separation between subband centers (vertical dashed lines).

Panels (e)-(h) present DOS_S and DOS_{As} from Eq.(10), which characterize the *symmetric* and *antisymmetric* spectral densities, respectively, in the presence of Weyl quasiparticles. These panels follow trends analogous to those of (a)-(d).

At the threshold $Q_{0d} = 0.16D$, DOS_{As} at the degeneracy point becomes significantly stronger than DOS_S . The enhancement of the amplitude of this resonant state originates from the off-diagonal DOS_{jl} at this energy, which acquires a large negative value [panel (c)]. For DOS_{As} , the interference term $-(\text{DOS}_{12} + \text{DOS}_{21})$ amplifies spectral weight, whereas for DOS_S , the sign-flipped term $+(\text{DOS}_{12} + \text{DOS}_{21})$ suppresses it.

Above the threshold ($Q_0 > Q_{0d}$), stronger IS break enhances spectral broadening in the *antisymmetric* (blueshifted) and *symmetric* (redshifted) components [panel (h)], with the latter being more pronounced. Simultaneously, the *symmetric* center shifts toward the lower (infrared $-D$) band cutoff, while the *antisymmetric* component approaches the Fermi energy from below. In the conduction band (not shown), this trend reverses: *antisymmetric* (redshifted) and *symmetric* (blueshifted) components shift toward the Fermi energy and upper (ultraviolet $+D$) band cutoff, respectively.

To elucidate this behavior, we explicitly show in Fig.3 the numerical solutions of Eq.(8) for the Q_0 - and J -dependent *antisymmetric* and *symmetric* subband centers for the cases of single ($J = 1$), double ($J = 2$) and triple ($J = 3$) Weyl fermions. This approach systematically tracks the evolution of the subband center as the IS is broken. Particularly, the degeneracy threshold Q_0 decreases with increasing J . For $J = 3$, the *antisymmetric* level asymptotically approaches the Fermi energy from below more rapidly than for $J = 1, 2$. Remarkably, *antisymmetric* centers persist near the Fermi energy as quasi-zero energy modes, indicating that orbitals of identical symmetry (e.g., *antisymmetric*-type) cannot achieve degeneracy even when Q_0 is extremely close to the energy cutoff D . Conversely, *symmetric*-type orbitals move progressively toward the infrared and ultraviolet band cutoffs, consistent with their suppressed spectral weight, and likewise fail to degenerate.

Conclusions- We demonstrated that *symmetric* and *antisymmetric molecular-like* subbands in a multi-Weyl semimetal dimer host novel quantum states in the IS

breaking regime. In the IS-preserved multi-Weyl phase, these subbands remain distinct. At a specific IS-breaking strength, the lifting of Weyl node degeneracy closes the *pseudogap*, and drives the system to a multi-Weyl metallic phase where the subband centers resonate. Beyond this threshold, *symmetric* subbands move toward infrared and ultraviolet band cutoffs, exhibiting spectral broadening and flattening, while *antisymmetric* subband centers asymptotically approach the Fermi level without crossing it, forming a pair of quasi-zero energy modes. These results provide deeper insights into quasiparticle mediated chemical bonding mechanisms in multi-Weyl systems, thereby highlighting a pathway to engineer novel molecular states in topological Weyl materials.

Acknowledgments- We thank the Brazilian funding agencies CNPq (Grants. Nr. 302887/2020-2, 303772/2023-9, 311980/2021-0, and 308695/2021-6), the São Paulo Research Foundation (FAPESP; Grant No. 2023/13467-6), Coordenação de Aperfeiçoamento de Pessoal de Nível Superior - Brasil (CAPES) – Finance Code 001 and FAPERJ process Nr. 210355/2018.

-
- [1] C. Fang, M. J. Gilbert, X. Dai, and B. A. Bernevig, *Phys. Rev. Lett.* **108**, 266802 (2012).
- [2] R. M. A. Dantas, F. Peña Benitez, B. Roy, and P. Surówka, *Phys. Rev. Research* **2**, 013007 (2020).
- [3] S.-M. Huang, S.-Y. Xu, I. Belopolski, C.-C. Lee, G. Chang, T.-R. Chang, B. Wang, N. Alidoust, G. Bian, M. Neupane, D. Sanchez, H. Zheng, H.-T. Jeng, A. Bansil, T. Neupert, H. Lin, and M. Z. Hasan, *Proceedings of the National Academy of Sciences* **113**, 1180 (2016).
- [4] Q. Liu and A. Zunger, *Phys. Rev. X* **7**, 021019 (2017).
- [5] N. P. Armitage, E. J. Mele, and A. Vishwanath, *Rev. Mod. Phys.* **90**, 015001 (2018).
- [6] J. Hu, S.-Y. Xu, N. Ni, and Z. Mao, *Annual Review of Materials Research* **49**, 207 (2019).
- [7] M. Z. Hasan, G. Chang, I. Belopolski, G. Bian, S.-Y. Xu, and J.-X. Yin, *Nature Reviews Materials* **6**, 784 (2021).
- [8] M. Z. Hasan, S.-Y. Xu, I. Belopolski, and S.-M. Huang, *Annual Review of Condensed Matter Physics* **8**, 289 (2017).
- [9] B. Yan and C. Felser, *Annual Review of Condensed Matter Physics* **8**, 337 (2017).
- [10] H. Zheng and M. Zahid Hasan, *Advances in Physics: X* **3**, 1466661 (2018).
- [11] T. Hayata, Y. Kikuchi, and Y. Tanizaki, *Phys. Rev. B* **96**, 085112 (2017).
- [12] Z.-M. Huang, J. Zhou, and S.-Q. Shen, *Phys. Rev. B* **96**, 085201 (2017).
- [13] A. Bharti and G. Dixit, *Phys. Rev. B* **107**, 224308 (2023).
- [14] S. Ahn, E. J. Mele, and H. Min, *Phys. Rev. B* **95**, 161112 (2017).
- [15] S. P. Mukherjee and J. P. Carbotte, *Phys. Rev. B* **97**, 045150 (2018).
- [16] S. Park, S. Woo, E. J. Mele, and H. Min, *Phys. Rev. B* **95**, 161113 (2017).
- [17] W. C. Silva, W. N. Mizobata, J. E. Sanches, L. S. Ricco, I. A. Shelykh, M. de Souza, M. S. Figueira, E. Vernek, and A. C. Seridonio, *Phys. Rev. B* **105**, 235135 (2022).
- [18] L. X. Fu and C. M. Wang, *Phys. Rev. B* **105**, 035201 (2022).
- [19] E. V. Gorbar, V. A. Miransky, I. A. Shovkovy, and P. O. Sukhachov, *Phys. Rev. B* **96**, 155138 (2017).
- [20] Q. Chen and G. A. Fiete, *Phys. Rev. B* **93**, 155125 (2016).
- [21] G. Xu, H. Weng, Z. Wang, X. Dai, and Z. Fang, *Phys. Rev. Lett.* **107**, 186806 (2011).
- [22] F. Xiong, C. Honerkamp, D. M. Kennes, and T. Nag, *Phys. Rev. B* **106**, 045424 (2022).
- [23] R. M. A. Dantas, F. Peña Benitez, B. Roy, and P. Surówka, *Journal of High Energy Physics* **2018**, 69 (2018).
- [24] S. Ghosh, S. Nandy, J.-X. Zhu, and A. Taraphder, *Phys. Rev. B* **109**, 045437 (2024).
- [25] S. Ghosh, S. Nandy, J.-X. Zhu, and A. Taraphder, *Phys. Rev. B* **109**, 045437 (2024).
- [26] H.-F. Lü, Y.-H. Deng, S.-S. Ke, Y. Guo, and H.-W. Zhang, *Phys. Rev. B* **99**, 115109 (2019).
- [27] A. K. Mitchell and L. Fritz, *Phys. Rev. B* **92**, 121109 (2015).
- [28] G. T. D. Pedrosa, J. F. Silva, and E. Vernek, *Phys. Rev. B* **103**, 045137 (2021).
- [29] J. F. Silva and E. Miranda, *Phys. Rev. B* **109**, 035153 (2024).
- [30] A. Kofuji, Y. Michishita, and R. Peters, *Phys. Rev. B* **104**, 085151 (2021).
- [31] Y.-W. Lu, P.-H. Chou, C.-H. Chung, and C.-Y. Mou, *Phys. Rev. B* **99**, 035141 (2019).
- [32] Y. Sun and A. Wang, *Journal of Physics: Condensed Matter* **29**, 435306 (2017).
- [33] H.-R. Chang, J. Zhou, S.-X. Wang, W.-Y. Shan, and D. Xiao, *Phys. Rev. B* **92**, 241103 (2015).
- [34] S. Verma, D. Giri, H. A. Fertig, and A. Kundu, *Phys. Rev. B* **101**, 085419 (2020).
- [35] G. C. Paul, S. F. Islam, P. Dutta, and A. Saha, *Phys. Rev. B* **103**, 115306 (2021).
- [36] H.-J. Duan, S.-M. Cai, X. Wei, Y.-C. Chen, Y.-J. Wu,

- M.-X. Deng, R. Wang, and M. Yang, *Phys. Rev. B* **109**, 205149 (2024).
- [37] J. Hubbard, *Proceedings of the Royal Society of London. Series A, Mathematical and Physical Sciences* **276**, 238 (1963).
- [38] H. Bruus and K. Flensberg, (Oxford: Oxford University Press) (2012).
- [39] L. H. Guessi, R. S. Machado, Y. Marques, L. S. Ricco, K. Kristinsson, M. Yoshida, I. A. Shelykh, M. de Souza, and A. C. Seridonio, *Phys. Rev. B* **92**, 045409 (2015).
- [40] P. W. Anderson, *Phys. Rev.* **124**, 41 (1961).